The Astrophysical Journal Letters, 973:L29 (9pp), 2024 September 20 https://doi.org/10.3847/2041-8213/ad772d

On the Kinematic Nature of Apparent Disks at High Redshifts: Local Counterparts are Not Dominated by Ordered Rotation but by Tangentially Anisotropic Random Motion

Bitao Wang[1,2], Yingjie Peng[2,3], Michele Cappellari[4], Hua Gao[5], and Houjun Mo[6,7]
[1] School of Physics and Electronics, Hunan University, Changsha 410082, People's Republic of China; bitao.wang@hnu.edu.cn
[2] Kavli Institute for Astronomy and Astrophysics, Peking University, Beijing 100871, People's Republic of China
[3] Department of Astronomy, School of Physics, Peking University, Beijing 100871, People's Republic of China
[4] Sub-department of Astrophysics, Department of Physics, University of Oxford, Denys Wilkinson Building, Keble Road, Oxford OX1 3RH, UK
[5] Institute for Astronomy, University of Hawaii, 2680 Woodlawn Drive, Honolulu, HI 96822, USA
[6] Department of Astronomy, University of Massachusetts, Amherst, MA 01003, USA
[7] Tsung-Dao Lee Institute, Shanghai Jiao Tong University, Shanghai 200240, People's Republic of China
Received 2024 May 19; revised 2024 August 31; accepted 2024 September 3; published 2024 September 18

Abstract

It is not straightforward to physically interpret the apparent morphology of galaxies. Recent observations by the James Webb Space Telescope (JWST) revealed a dominant galaxy population at high redshifts ($z > 2$) that were visually classified as disks for their flattened shapes and/or exponential light profiles. The extensively accepted interpretation is that they are dynamically cold disks supported by bulk rotation. However, it is long known that flattened shapes and exponential profiles are not exclusive for rotating disk structure. To break degeneracy and assess the rotational support of typical high-z galaxies in the JWST samples, those with active star formation and stellar masses $\lg(\mathcal{M}_\star/\mathcal{M}_\odot) \sim 9$, we study the kinematics of their equal-mass counterparts at $z = 0$. While these local star-forming low-mass galaxies are photometrically similar to real dynamically cold disks, they are not supported by ordered rotation but primarily by random motion, and their flattened shapes result largely from tangential orbital anisotropy. Given the empirical and theoretical evidence that young galaxies are dynamically hotter at higher redshifts, our results suggest that the high-z JWST galaxies may not be cold disks but are dynamically warm/hot galaxies with flattened shapes driven by anisotropy. While both have low rotational support, local low-mass galaxies possess oblate shapes, contrasting the prolate shapes (i.e., cigar like) of low-mass systems at high redshifts. Such shape transition (prolate $\Rightarrow$ oblate) indicates an associated change in orbital anisotropy (radial $\Rightarrow$ tangential), with roots likely in the assembly of their host dark matter halos.

Unified Astronomy Thesaurus concepts: Extragalactic astronomy (506)

1. Introduction

Over the course of understanding galaxy populations in the Universe, it has been a long-lasting pursuit to measure the intrinsic three-dimensional shapes and the internal kinematics of galaxies.

It was not widely realized until the 1920s that galaxies are stellar systems beyond the confine of our Milky Way. Just a decade after, Hubble's morphological classification scheme was introduced (E. P. Hubble 1936) and has been serving as the basis even for modern studies related to galaxy morphology. Hubble's classifications acknowledge the diversity in galaxy intrinsic shapes, in the sense that early-type elliptical galaxies are more spheroidal in three dimensions (i.e., large minor-to-major axis ratios) and late-type spiral galaxies are oblate disks (A. Sandage et al. 1970). The existence of intrinsically spheroidal galaxies is supported by the fact that the distribution of projected galaxy ellipticity in the local Universe contains too many round objects to be explained by randomly oriented disks alone (E. P. Hubble 1926).

With statistical analyses of projected shapes of galaxies and their subcomponents (e.g., N. D. Padilla & M. A. Strauss 2008; A. van der Wel et al. 2009; R. Sánchez-Janssen et al. 2010; S. Rodríguez & N. D. Padilla 2013; H. Gao et al. 2020; D. Xu et al. 2024) and of stellar kinematics (e.g., D. Krajnović et al. 2011; E. Emsellem et al. 2011; M. Cappellari et al. 2013b), now it is generally believed that local galaxy populations dominant in mass are mainly axisymmetric oblate and spheroidal systems and that the most massive early-type galaxies are mildly triaxial (A.-M. Weijmans et al. 2014; H. Li et al. 2018). The fast-rotating oblate and slow-rotating spheroidal/ellipsoidal galaxies manifest a bimodal distribution of their rotational support (M. Cappellari 2016; M. T. Graham et al. 2018; J. van de Sande et al. 2021b), which has recently been shown to be a universal property for galaxies across different masses, star formation states, and environments (B. Wang & Y. Peng 2023; B. Wang et al. 2023).

At redshift $z \sim 0$, dynamically hot spheroidal/ellipsoidal galaxies only make up the minority unless galaxies are overly massive ($\mathcal{M}_\star \gtrsim 10^{11}\mathcal{M}_\odot$) and with relatively low star formation rates (SFRs; B. Wang et al. 2020; A. Fraser-McKelvie et al. 2021). Modern simulations predict that hot spheroids are much more prevalent at higher redshifts before the cosmic noon $z > 2$, when even the star-forming galaxies are generally far from being dynamically cold (EAGLE, TNG100, TNG50; A. Pillepich et al. 2019; J. W. Trayford et al. 2019; S. Tacchella et al. 2019). The advent of the James Webb Space Telescope (JWST) has recently enabled tests in the high-redshift Universe, with its unprecedented resolution and sensitivity at infrared wavelengths desirable for probing stellar structures. However, several latest works using JWST data show seemingly the opposite to the simulations: visually identified

disk galaxies (of typical flattened shapes and nearly exponential surface brightness profiles) dominate the galaxy populations beyond cosmic noon (e.g., J. S. Kartaltepe et al. 2023; L. Ferreira et al. 2023; W. Sun et al. 2024). These empirical results have been extensively interpreted as that rotation-supported and dynamically cold galaxies are prevailing even at high redshifts. If such an interpretation is right, galaxy formation theories in high-density regimes may need to be revised.

Nevertheless, inferring the intrinsic morphology and kinematics from imaging alone is inherently uncertain. Particularly, the flattened shapes of galaxies, which have been deemed indicative of disks in visual morphological classifications, do not necessarily guarantee rotating oblate disk structures. In addition to ordered rotation, flattening can also be caused by the anisotropy of random motion. This is the case among nearby giant elliptical galaxies, which were originally thought to be flattened by rotations but later found to be by velocity anisotropy (F. Bertola & M. Capaccioli 1975; J. Binney 1976, 1978; G. Illingworth 1977). When projected on the sky, elongated galaxies of intrinsic prolate shapes, dynamically supported by radial motions, tend to show themselves in flattening seemingly like the edge-on disks (e.g., D. Ceverino et al. 2015).

Without deep integral field spectroscopy, it cannot be pinned down whether the prevailing high-z disks are actually supported by anisotropic random motion. But before that consuming data, in this work we study the stellar kinematics of local galaxies with masses comparable to those of the typical high-z galaxies observed by JWST ($\lg(\mathcal{M}_\star/\mathcal{M}_\odot) \sim 9$). This sets a benchmark of the rotational support of low-mass systems in relatively quiescent formation, providing key information for assessing the case at high z when galaxy assembly is substantially more violent. In the last section, we bring together other pieces of evidence from observations and simulations to discuss the nature of these high-z flattened galaxies.

Throughout this work we adopt the concordance cosmology with $H_0 = 70\,\mathrm{km\,s^{-1}\,Mpc^{-1}}$, $\Omega_\mathrm{m} = 0.3$, and $\Omega_\Lambda = 0.7$.

2. Sample

The local galaxy samples to be compared with high-z galaxies are drawn from the complete MaNGA survey (K. Bundy et al. 2015; Abdurro'uf et al. 2022), which ensures better understanding of galaxy shapes with integral field spectroscopy. MaNGA has observed ∼10,000 galaxies, the largest survey of the kind, in the local Universe ($0.01 < z < 0.15$) at angular resolution $2\farcs5$ in FWHM with the integral field units of effective diameters ranging from $12''$ to $32''$ (N. Drory et al. 2015). This spatial coverage in most cases ensures observations out to at least 1.5 effective radii of the galaxies. The spectra cover 360–1030 nm with median instrument broadening $\sigma_\mathrm{inst} \sim 72\,\mathrm{km\,s^{-1}}$ (D. R. Law et al. 2016) and typical spectral resolution $R \sim 2000$.

We use the spin parameter λ_{R_e} (E. Emsellem et al. 2007), the effective specific angular momentum of stars, to quantify the rotational support of galaxies and to constrain their intrinsic shapes. The robust λ_{R_e} measurements for the complete MaNGA sample are described in B. Wang & Y. Peng (2023). We apply careful quality control to remove systems with spectroscopic or photometric problems and to exclude merging galaxies in chaotic morphology for which quantification of internal kinematics is not attainable (see more details in B. Wang & Y. Peng 2023). The smearing of rotation field by seeing is corrected for using the analytic functions derived in M. T. Graham et al. (2018), which has been tested in simulations (K. E. Harborne et al. 2019) showing the correction is effective with little systematics.

The flattening of the apparent galaxy shapes is quantified via ellipticity ε, i.e., $1 - b/a$, inside the half-light isophote. Ellipticity ε together with the position angle of photometric major axis $\mathrm{PA_{phot}}$ are determined via Multi-Gaussian Expansion[8] (E. Emsellem et al. 1994) modeling of the SDSS r-band surface brightness maps. The position angle of kinematic major axis $\mathrm{PA_{kine}}$ is defined by the axis aligned with the main sense of rotation in the stellar mean velocity field, which is measured by using PAFIT[9] (D. Krajnović et al. 2006). We take the values of ellipticity and the two position angles from the catalog[10] of K. Zhu et al. (2023). The Sérsic indices measured for MaNGA galaxies using SDSS optical images are taken from the PyMorph photometric catalog[11] (J.-L. Fischer et al. 2019; H. Domínguez Sánchez et al. 2022).

We retrieve total stellar mass and SFR for MaNGA galaxies from the version X2 of GALEX-SDSS-WISE Legacy Catalogue[12] (GSWLC-X2; S. Salim et al. 2016, 2018), which are derived by modeling the ultraviolet, optical, and mid-infrared fluxes.

Among the representative local galaxy populations sampled by the MaNGA survey, we cull the following two subsamples for our purpose of suggesting the probable disconnection between exponential flattened shapes and cold rotating disks in JWST high-z galaxies.

Low-mass galaxies at $z = 0$: These are 149 MaNGA galaxies in a narrow stellar mass bin $8.9 < \lg(\mathcal{M}_\star/\mathcal{M}_\odot) < 9.1$ with robust measurements of stellar spin λ_{R_e}. Their low masses are comparable to the median masses of JWST high-z samples studied in J. S. Kartaltepe et al. (2023) and L. Ferreira et al. (2023), thus making them local analogs (in terms of stellar mass) of typical JWST galaxies found in the early Universe. No environment restriction is applied. Because these low-mass galaxies are in the low-luminosity regime of the MaNGA sample, they are predominantly actively star forming (the same also for JWST galaxies). The images and maps of mean velocity and velocity dispersion have been visually checked to make sure the photometric and kinematic measurements are sensible. We note that the uncertainty in estimating the velocity dispersion below the instrument resolution has been largely reduced (M. Cappellari 2017). For some pixels, the intrinsic velocity dispersion of stars is negligible, and the broadening of spectral features is predominantly due to the limited velocity resolution of the instrument, leading to estimated quadratic velocity dispersion that is unphysically negative. The velocity dispersion values in such pixels have been set to zero. Despite the uncertainty in measuring these intrinsically low values of velocity dispersion, such pixels are quite minor and unimportant in the low-mass sample because at median value they only comprise ∼4% of all pixels within the area for calculating λ_{R_e}.

[8] Using the MGEFIT Python software package of M. Cappellari (2002) available at https://pypi.org/project/mgefit/.
[9] Available at https://pypi.org/project/pafit/.
[10] https://manga-dynpop.github.io
[11] https://www.sdss4.org/dr17/data_access/value-added-catalogs/?vac_id=manga-pymorph-dr17-photometric-catalog
[12] https://salims.pages.iu.edu/gswlc/

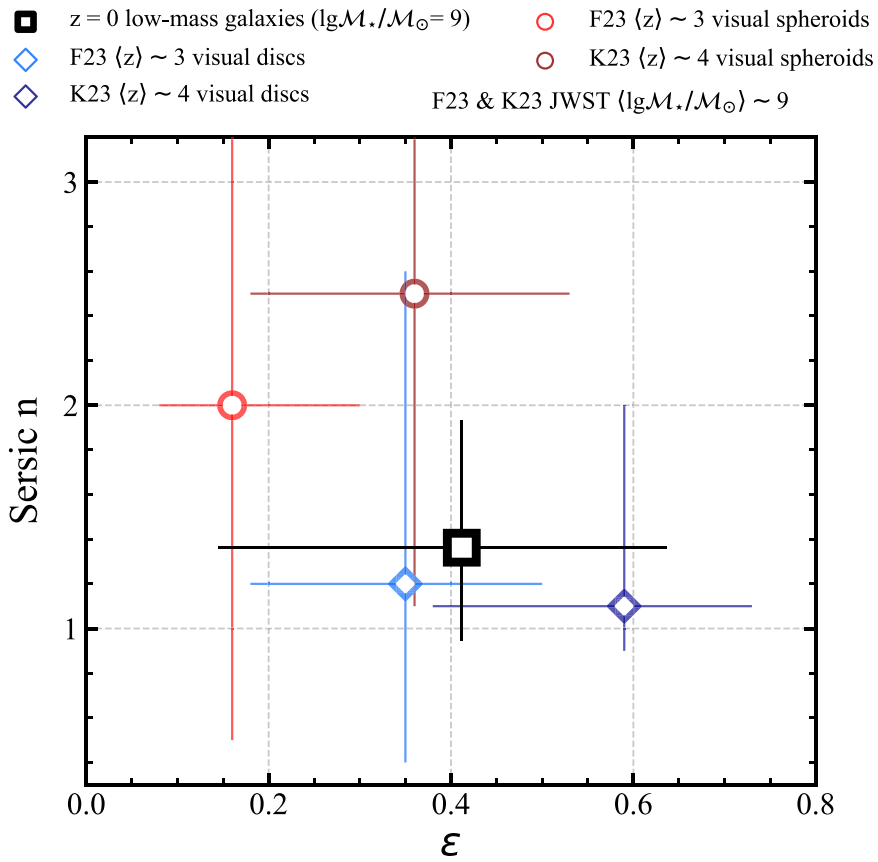

Figure 1. The concentration of rest-frame optical surface brightness profiles, as quantified by Sérsic indices, vs. the ellipticity ε (i.e., flattening or fractional axial difference $1-b/a$) of optical isophotes. The red and blue symbols mark the medians and 16th–84th percentiles of JWST visually identified spheroids and disks, respectively, from K23 and F23, while the black symbol is for low-mass galaxies in the local Universe observed in the MaNGA survey. The stellar masses of these low-mass galaxies at $z=0$ are typical in the JWST samples.

Milky Way analogs at $z=0$: We also select Milky Way analogs in the MaNGA survey to represent the real dynamically cold disks in the local Universe. These 221 analogs are defined by stellar mass range $10.6<\lg(\mathcal{M}_\star/\mathcal{M}_\odot)<10.8$ (around the median of the estimated range in A. Pillepich et al. 2023) and are confined within the span of the star formation main sequence (SFMS) of local galaxies (Section 2.1 of B. Wang & Y. Peng 2023). We do not additionally apply any morphology cut as these galaxies are already overwhelmed by fast-rotating disks with high rotational support (B. Wang et al. 2023).

3. The Projection of Ellipsoids

To get a first-order assessment of galaxy intrinsic shapes, later in this Letter we will see distributions of the ellipticity ε of galaxy-projected shapes as compared to the analytic predictions for projected ellipsoids.

The projection of a general ellipsoid with three principal axes, $c\leqslant b\leqslant a$, and two axial ratios, $\xi\equiv c/a$ and $\zeta\equiv b/a$, is described in J. Binney (1985), and for convenience we summarize the relevant part below.

The projected axial ratio q (i.e., $1-\varepsilon$) is given by

$$q(\theta,\,\phi;\,\xi,\,\zeta)=\left[\frac{A+C-\sqrt{(A-C)^2+B^2}}{A+C+\sqrt{(A-C)^2+B^2}}\right]^{1/2}, \quad (1)$$

where $(\theta,\,\phi)$ define the line of sight and are the polar angle and azimuthal angle with respect to the shortest and longest axis, respectively, and

$$A\equiv\frac{\cos^2\theta}{\xi^2}\left(\sin^2\phi+\frac{\cos^2\phi}{\zeta^2}\right)+\frac{\sin^2\theta}{\zeta^2}, \quad (2)$$

$$B\equiv\cos\theta\,\sin 2\phi\left(1-\frac{1}{\zeta^2}\right)\frac{1}{\xi^2}, \quad (3)$$

$$C\equiv\left(\frac{\sin^2\phi}{\zeta^2}+\cos^2\phi\right)\frac{1}{\xi^2}. \quad (4)$$

4. Results

The JWST CEERS survey (S. L. Finkelstein et al. 2023) has imaged thousands of high-z galaxies in the rest-frame optical in the redshift range $2<z<5$ mainly with stellar masses $8<\lg(\mathcal{M}_\star/\mathcal{M}_\odot)<10$. Statistical analyses of stellar structure show high fractions of galaxies with flattened shapes and low concentrations (nearly exponential profiles), which tend to be visually classified as "disks."

In Figure 1, we illustrate the galaxy distributions on the Sérsic n versus the ellipticity parameter plane. The red and blue symbols mark the medians and 16th–84th percentiles of JWST visually identified spheroids and disks, respectively, extracted from two representative works (J. S. Kartaltepe et al. 2023; L. Ferreira et al. 2023, abbreviated as K23 and F23 hereafter, respectively). The sample studied by K23 is restricted to higher redshifts ($z>3$) and larger stellar masses ($9<\lg(\mathcal{M}_\star/\mathcal{M}_\odot)$).

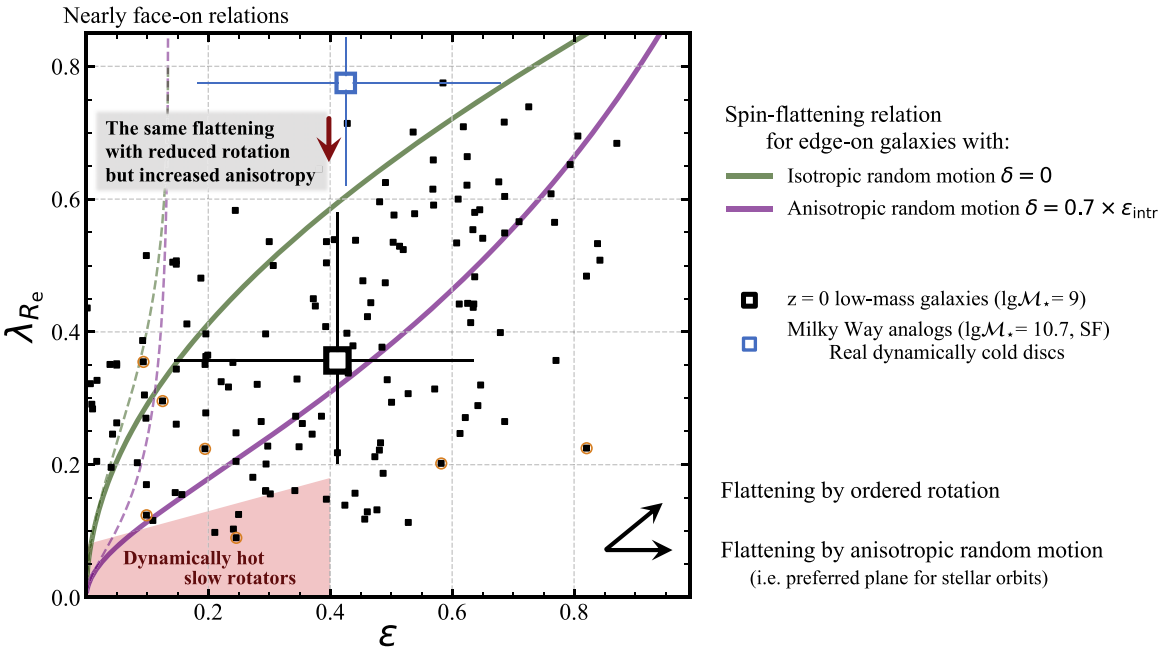

Figure 2. The stellar spin λ_{R_e} vs. flattening ε, indicating the overall warm/hot stellar kinematics of low-mass galaxies in the local Universe. The large black square and error bars denote the median and 16th–84th percentiles of the low-mass sample, respectively, each galaxy of which is shown by a small black square. The most actively star-forming ones (0.5 dex above the SFMS) are circled in orange, and among local low-mass galaxies they can be better analogs of high-z low-mass systems for further similarity in star formation and gas properties. For comparison, Milky Way analogs in the local Universe, as representatives of real dynamically cold thin disks, are shown by the large blue square, and the area occupied by dynamically hot slow rotators is illustrated by the shaded trapezoid. The green and magenta solid curves are loci, respectively, for isotropic and anisotropic edge-on axisymmetric galaxies, predicted by tensor virial theorem, with anisotropy in the stellar random motion as given by the relations $\delta = 0$ and $\delta = 0.7\varepsilon_{\rm intr}$. The relations for nearly face-on (at an inclination angle of 30°) rotators are shown by the green and magenta dashed curves. We note that roughly half of low-mass galaxies distribute below the magenta solid curve, suggesting that they are significantly more anisotropic than galaxies of higher stellar masses that lie mostly above the magenta solid curve. The suggested high anisotropy of low-mass galaxies explains their flattened shapes at low levels of rotation.

The morphological classifications are also more detailed in K23, and we pick their "disk-only" objects to represent the population that seem to be dominated by disk structure. There are systematic offsets between the K23 and F23 results, while in general visually classified disks have lower Sérsic indices and more flattened shapes. The black symbol shows the distributions for low-mass galaxies in the local Universe, which overlap mostly with the two JWST visual disk populations. If these low-mass galaxies at $z = 0$ were analyzed using images at spatial resolution (e.g., the FWHM of the point-spread function normalized by galaxy size) comparable to that of JWST galaxies, many of them may also tend to be visually classified as "disks."

However, the measurements of stellar spin indicate that these low-mass galaxies at $z = 0$ are dynamically too hot with too little rotational support to be considered a population of cold rotating disks. Figure 2 shows the observed galaxy distributions and theoretical predictions on the λ_{R_e} versus ε (stellar spin versus flattening) diagram. Again, the large black square and associated error bars are the median and 16th–84th percentiles of low-mass galaxies at $z = 0$, respectively, while small black squares stand for individual galaxies. For low-mass galaxies, the median magnitude of stellar spin is 0.35, meaning that the specific angular momenta of these systems are only about one-third of the cases when they are maximally rotation supported. In terms of rotational support, they are closer to being dynamically hot slow rotators (e.g., giant elliptical galaxies) that occupy the lower-left area (M. Cappellari 2016) on the λ_{R_e} versus ε plane than being real thin disky galaxies like Milky Way analogs (the blue square).

Despite much less rotation, low-mass galaxies are still in shapes that look similarly flattened as those dynamically cold disks, as indicated by their entirely overlapped percentiles of ε distributions. This suggests that low-mass galaxies at $z \sim 0$ are flattened, to a large extent, by the anisotropy in random motion.

In Figure 2, we show how λ_{R_e} varies with ε, as predicted[13] by the tensor virial theorem (J. Binney 2005) for edge-on axisymmetric galaxies at different velocity anisotropy: The green solid curve is for isotropic rotators, i.e., those that have equivalent random motion along different directions, and it shows the steady increase of the flattening and rotational support in tandem (i.e., ↗ trend on the λ_{R_e}–ε diagram: flattening by ordered rotation). The magenta solid curve is for extreme anisotropy observed among more massive galaxies with $\lg(\mathcal{M}_\star/\mathcal{M}_\odot) > 9.5$, following the anisotropy relation of $\delta = 0.7\varepsilon_{\rm intr}$ (M. Cappellari et al. 2007), where $\varepsilon_{\rm intr}$ is ε viewed edge on. The global anisotropy parameter is defined as $\delta \equiv 1 - (\sigma_z/\sigma_x)^2$, with z aligned with the symmetry axis of the axisymmetry of galaxies and x being any direction orthogonal to it. At a given rotation, galaxies can be further flattened by increased anisotropy (→ trend), or the same flattening can be achieved with reduced rotation but increased anisotropy (↓ trend). Projection lowers both λ_{R_e} and ε, and the isotropic and anisotropic relations at an inclination angle of 30° are shown separately by the green and magenta dashed curves, respectively.

[13] See Equations (14)–(15) of M. Cappellari (2016). The prediction of λ_R uses the tight relation between λ_R and V/σ derived from observations and two-integral Jeans models (E. Emsellem et al. 2011, Equation (B1)), which have been checked for the low-mass MaNGA galaxies.

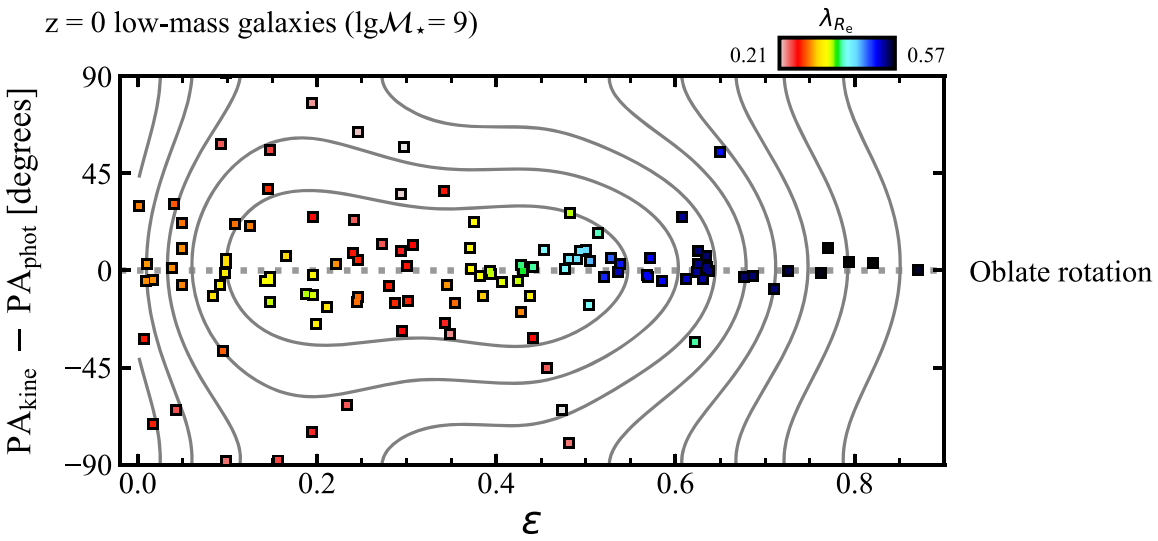

Figure 3. The misalignment ($PA_{kine} - PA_{phot}$) between the kinematic and photometric major axis as a function of ellipticity ε for MaNGA low-mass galaxies at $z = 0$, color coded by stellar spin λ_{R_e} (slightly smoothed using the locally weighted regression method LOESS by W. S. Cleveland & S. J. Devlin 1988, as implemented by M. Cappellari et al. 2013a; the Python package LOESS is available at https://pypi.org/project/loess/). The measurements of the position angles of the two axes are detailed in the text. The gray contour lines show the Gaussian kernel-estimated density of galaxies, and to avoid edge effects and account for the periodicity of angles, we have utilized two more duplicates of the data points shifted by ±180°. Taking measurement uncertainty into account, the distribution is consistent with the case of oblate rotators that have aligned kinematic and photometric major axes.

In the local Universe, unlike galaxies of these low masses $\lg(\mathcal{M}_\star/\mathcal{M}_\odot) \sim 9$, more massive galaxies with regular rotation field are well confined above the magenta solid curve (M. Cappellari et al. 2007; J. van de Sande et al. 2018; B. Wang et al. 2020), suggesting this curve to be an empirical anisotropy upper limit. Rare exceptions are those that manifest two peaks in the velocity dispersion field, which reveal the presence of two counterrotating disk components (D. Bevacqua et al. 2022). This empirical anisotropy upper limit (i.e., the magenta solid curve) also applies to the Milky Way analogs here, whose distribution can be described as oblate rotators with anisotropy in the range $[0, 0.7\varepsilon_{intr}]$ projected at random inclinations.

But at masses as low as $\lg(\mathcal{M}_\star/\mathcal{M}_\odot) \sim 9$, there appears to be a large fraction that break this empirical anisotropy upper limit and lie much below the magenta solid line. Using the theoretical zero rotation limit[14] (i.e., flattening is totally due to anisotropy; theoretically maximal anisotropy $\delta_{max}(\varepsilon_{intr})$ at given ε_{intr}) as a reference, the anisotropy relation $\delta(\varepsilon_{intr}) = 0.7\varepsilon_{intr}$ assumed by the magenta solid line approximates 80% of $\delta_{max}(\varepsilon_{intr})$, which represents the extreme among more massive galaxies. The distribution lower boundary of low-mass galaxies suggests that their anisotropy extreme approaches 99% of $\delta_{max}(\varepsilon_{intr})$, close to the zero rotation limit. Without the intention of overfitting the data, we tentatively build a mock sample of randomly oriented axisymmetric galaxies with ε_{intr} uniformly sampled in the range [0.4, 0.95] and anisotropy δ uniformly sampled in $[0.7\varepsilon_{intr}, 0.99\delta_{max}]$. The distribution of this mock sample on the λ_{R_e}–ε diagram largely resembles the observed distribution of the low-mass galaxies. Kolmogorov–Smirnov tests[15] suggest that it is very likely (p-value: 0.4–0.5) that these mock and real samples are drawn from the same underlying distribution. The tests rule out the possibility that most of the low-mass galaxies have anisotropy δ smaller than $0.7\varepsilon_{intr}$, which is also clearly indicated by the distribution showing half of them below the magenta solid line.

Such high anisotropy in the random motion explains the significant flattening of low-mass galaxies at low levels of stellar rotation. Under the assumption of oblate velocity ellipsoid (i.e., $\sigma_\phi \approx \sigma_R$), which is reasonable for more massive regular-rotator galaxies with $\lg(\mathcal{M}_\star/\mathcal{M}_\odot) > 9.5$ (M. Cappellari et al. 2007; M. Cappellari 2016), B. Wang et al. (2021) finds that, beyond this empirical anisotropy upper limit, the solutions to axisymmetric Jeans equations are unphysical in realistic galaxy potentials. This suggests that real galaxies can hardly establish hydrostatic equilibrium at that large anisotropy without biased stellar motion on the equatorial plane. Here, the fact that this empirical upper limit does not hold for low-mass galaxies implies that these low-mass galaxies, many of which show irregularity in the velocity field, tend to possess the nonoblate velocity ellipsoid ($\sigma_\phi \not\approx \sigma_R$) observed among galaxies with nonregular rotation (Figure 11 of M. Cappellari 2016).

Different types of orbital anisotropy can lead to different intrinsic shapes. Figure 3 shows that the photometric and kinematic major axes[16] of local low-mass galaxies are statistically aligned with each other, with expected large scatter around zero $PA_{kine} - PA_{phot}$ at low ε when the photometric major axis is not well defined. If galaxies are intrinsically prolate or triaxial, the photometric and kinematic major axes are not usually aligned, and the general alignment observed among the local low-mass galaxies indicates their overall oblate shapes in axisymmetry (see a more detailed review in Section 3.3 of M. Cappellari 2016).

The oblate shapes and large velocity anisotropy of these local low-mass systems mean that they have a substantial amount of kinetic energy of random motion along the equatorial plane in either the radial or tangential direction. Mergers are commonly found reasons for radial anisotropy on

[14] See the black dashed line in Figure 3 of B. Wang et al. (2021).

[15] The Python implementation of the two-dimensional Kolmogorov–Smirnov testing NDTEST is available at https://github.com/syrte/ndtest.

[16] Both position angles have been visually checked to exclude clearly unreliable measurements, such as those due to a large area of low signal-to-noise ratio in the velocity maps.

galactic scales, such as for the Gaia Enceladus (V. Belokurov et al. 2018) in the Milky Way, but are of limited importance in low-mass galaxies due to their low ex situ mass fractions (e.g., S. Tacchella et al. 2019). Moreover, fine-tuned merger configuration might be required to confine the accreted stars in the equatorial plane. Tangentially biased orbits ($\sigma_\phi > \sigma_R$), on the other hand, like the special cases of significant counter-rotating disks seen among more massive galaxies (Figure D1 of B. Wang et al. 2020 in the appendix), are seemingly more realistic and practical for the shapes and anisotropy of these local low-mass galaxies. Due to frequent angular momentum changes of the feeding cosmic-web streams, the spin axes of gas disks in low-mass galaxies flip in less than an orbital time (A. Dekel et al. 2020). Therefore, low-mass galaxies may indeed host significant counterrotating stellar populations. However, we note that their small intrinsic velocity dispersion is well below the MaNGA instrumental dispersion, as well as the spatially overlapping counterrotation after multiple spin flips, make the counterrotating signals hard to reveal from the velocity and dispersion maps.

With their particular properties, the local low-mass galaxies form another significant population below the magenta line in Figure 2, in addition to the widely acknowledged massive slow-rotator populations that are made by a series of major and minor dry mergers. In the following section, we will bring more discussion on these two populations below the magenta line.

5. Discussion and Conclusion

In this work, we learn from the stellar kinematics and shapes of low-mass, $\lg(\mathcal{M}_\star/\mathcal{M}_\odot) \sim 9$, galaxies in the local Universe. These low-mass systems, mostly star forming, have nearly exponential profiles of surface brightness and apparent shapes that are comparably flattened as dynamically cold disky galaxies like our Milky Way. Such photometric features are closely related to the presence of dominant disk structures in more massive populations at $z = 0$. This link, however, is not guaranteed unconditionally. We show that these low-mass galaxies, which may be visually classified as disks according to their photometric features, are actually much more dominated by stellar random motion than those real rotation-supported disks, and their apparent flattening is attributed to high anisotropy in the random motion. The anisotropy is most likely to be tangential, i.e., stellar orbits are tangentially biased, so as to account for the intrinsic oblate shapes of these local low-mass galaxies indicated by the general alignment between their photometric and kinematic major axes.

Below the empirical anisotropy relation (i.e., the magenta line in Figure 2) for the axisymmetric oblate regular rotators dominating in the local Universe, the primary population are slow-rotator early-type galaxies at the very high-mass end $\lg(\mathcal{M}_\star/\mathcal{M}_\odot) \gtrsim 11$ (M. Cappellari 2016; M. T. Graham et al. 2018; B. Wang et al. 2020; J. van de Sande et al. 2021a). The formation of low-mass galaxies with high tangential anisotropy gives rise to another prominent population below the relation at the low-mass end $\lg(\mathcal{M}_\star/\mathcal{M}_\odot) \sim 9$. The massive ones are formed[17] by a number of major and minor dry mergers, evidenced by their slightly triaxial shapes (M. Cappellari et al. 2007; E. Emsellem et al. 2011; G. Santucci et al. 2022), central stellar cores (J. Kormendy & R. Bender 1996; S. M. Faber et al. 1997; D. Krajnović et al. 2020), extremely low bulk rotation, massive and extended stellar halos, environment (e.g., M. Cappellari 2013; B. Wang et al. 2020; J. van de Sande et al. 2021a; G. Santucci et al. 2023), and others. The low-mass ones, in spite of low angular momenta, still retain the oblate shapes that might be the consequence of multiple spin flips of the gas disks (A. Dekel et al. 2020). Spectra of higher velocity resolution are needed to resolve the underlying counterrotating stars in these systems of low-velocity dispersion.

Studying kinematics of low-mass galaxies in the local Universe serves as an invaluable proxy for understanding their counterparts recently studied photometrically at high redshift. Beyond cosmic noon $z > 2$, JWST images have revealed a dominating population of galaxies with flattened shapes and nearly exponential surface brightness profiles. Visual morphological studies classify these galaxies as a disk population, and it is widely believed that many of them are dynamically cold disks supported by bulk rotation. However, we note that the high-z JWST galaxies are mainly star forming and have typical stellar masses (i.e., the median) of $\lg(\mathcal{M}_\star/\mathcal{M}_\odot) \sim 9$, thus making them distant counterparts of the local populations presented in this work. While we show that the local low-mass populations are also significantly flattened and have nearly exponential profiles, they are no where near being rotation-supported systems.

From a theoretical point of view, the stellar kinematics of actively star-forming galaxies at higher redshifts are governed more by random motion than their local analogs of equal masses (EAGLE, TNG100, TNG50; A. Pillepich et al. 2019; J. W. Trayford et al. 2019; S. Tacchella et al. 2019) because the fast accumulated gas becomes gravitationally unstable toward star formation far ahead of complete gas cooling and settling down into a disk (H. Mo et al. 2024). This is consistent with observations that molecular and ionized gas, which stay closely with young stars, are dynamically hotter at higher redshifts (e.g., E. Wisnioski et al. 2015). Significant rotation of cool and cold gas can still be established at extremely high redshifts (e.g., L. E. Rowland et al. 2024; S. Fujimoto et al. 2024), particularly for massive halos as the simulation suggested, but tends to be fragile and destructed after several orbital time (A. Dekel et al. 2020).

The typical JWST galaxies observed at high z are thus expected to be supported even more by random motion than the local equal-mass counterparts highlighted in this work, which were formed recently and quiescently. For the local counterparts, if we focus on those with the highest SFRs (0.5 dex above the SFMS; orange circles in Figure 2), which are more analogous to the high-z population in terms of star formation and gas properties, the median stellar spin does decrease further by 40%.

There are indeed other pieces of evidence for high-z star-forming galaxies being dynamically warm/hot systems with large velocity anisotropy. Most notably, high-z galaxies of relatively low masses feature an asymmetric distribution of projected axis ratio that is biased toward small values. This is the characteristic of intrinsically elongated systems. H. Zhang et al. (2019) infer the intrinsic shapes of galaxies by modeling the projected axis ratios and sizes based on HST images and find that in the redshift range $2 < z < 2.5$, 70% of $9 < \lg(\mathcal{M}_\star/\mathcal{M}_\odot) < 9.5$ galaxies and 60% of $9.5 < \lg(\mathcal{M}_\star/\mathcal{M}_\odot) < 10$ galaxies are prolate, and the disky populations comprise fewer than 20%. The prevalence of low-mass prolate galaxies at high redshifts is confirmed by the latest

[17] A nonmerger origin may exist but is rare (e.g., C. d. P. Lagos et al. 2022).

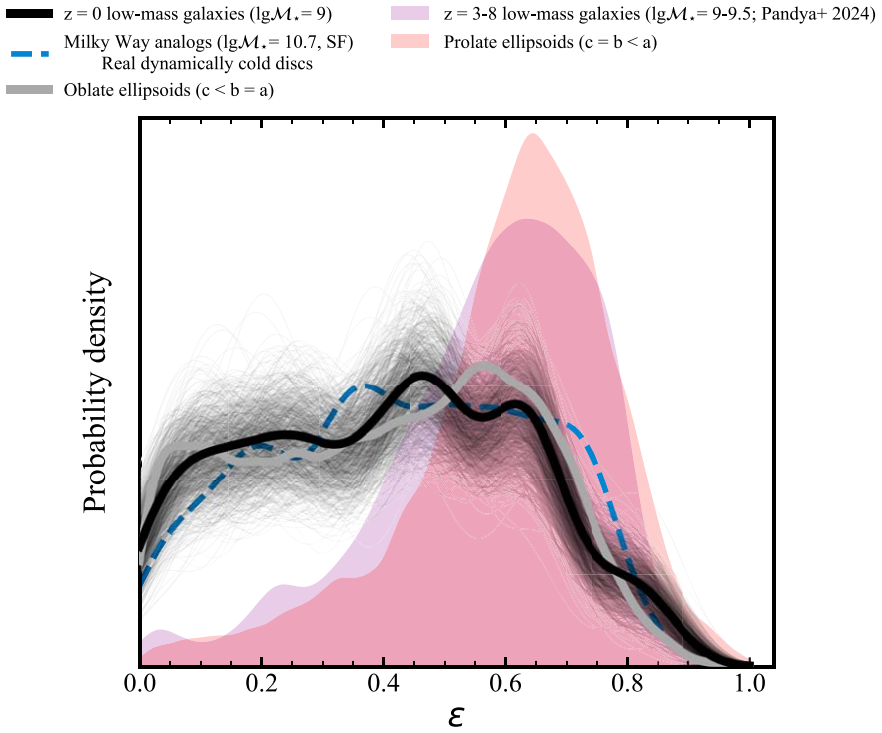

Figure 4. The probability density distributions of the ellipticity ε of galaxy-projected shapes for low-mass galaxies (black solid line) and Milky Way analogs (blue dashed line) observed at $z = 0$ and for galaxies in the early Universe $z = 3-8$ ($9 < \lg(\mathcal{M}_\star/\mathcal{M}_\odot) < 9.5$ in JWST CEERS studied by V. Pandya et al. 2024b; the purple shaded area). The density distributions are derived via kernel density estimation with Gaussian kernels of widths determined based on Scott's rule. For local low-mass galaxies, we estimate the uncertainty of the distribution using 1000 bootstrap samples shown by the thin black lines. Suggesting the intrinsic shapes to first order, we have also shown the predicted distributions of oblate ($c < b = a$, $c/a \sim \mathcal{N}(\mu = 0.3, \sigma = 0.1)$; the thick gray line) and prolate ($c = b < a$, $c/a \sim \mathcal{N}(\mu = 0.3, \sigma = 0.1)$; the orange shaded area) ellipsoids randomly projected on the sky plane.

JWST results (V. Pandya et al. 2024b), showing that about 70% of $9 < \lg(\mathcal{M}_\star/\mathcal{M}_\odot) < 10$ galaxies are prolate at $2 < z < 8$. V. Pandya et al. (2024b) also find that high-probability prolate and oblate candidates have remarkably similar Sérsic indices around one and nonparametric morphological properties. With integral field spectroscopy, our work suggests that these prolate systems, unlike rotation-supported disks in oblate shapes, are governed by anisotropic random motion.

The prolate shapes of high-z low-mass galaxies can naturally be rooted in the shapes and kinematics of their dark matter halos (A. C. R. Thob et al. 2019). Simulated low-mass galaxies at high z generally possess elongated prolate shapes, due to the gravitational impact from a dominant dark matter filament that feeds the central galaxy (D. Ceverino et al. 2015; M. Tomassetti et al. 2016), whose torque efficiently drives stars to anisotropic hot orbits. Recently, J. Vega-Ferrero et al. (2024) show that, with a self-supervised learning algorithm, a machine identifies a significant fraction of JWST visually classified disk galaxies as systems similar to the mock TNG50 galaxies with prolate shapes and low angular momenta. High-z galaxies, including these elongated systems, often show clumpy morphologies of luminous subcomponents that suggest early galaxy formation via frequent mergers (e.g., A. Adamo et al. 2024; Y. Harikane et al. 2024). The clumpiness of some of the elongated galaxies thus might indicate their temporary states far from equilibrium and that their prolate shapes are under fast evolution.

Both having low rotational support, the intrinsic shapes of low-mass galaxies with $\lg(\mathcal{M}_\star/\mathcal{M}_\odot) \sim 9$ have transitioned from prolate at $z > 2$ to oblate at present. Figure 4 illustrates this transition with the ellipticity distributions of local ($z = 0$; black line) and distant ($z = 3-8$; purple shaded area; taken from V. Pandya et al. 2024b) low-mass galaxies. Apparently, the projected shapes of local and distant low-mass galaxies are significantly different, with the distant low-mass galaxies showing much more highly flattened shapes on the sky. The distribution of local low-mass galaxies follows that of the Milky Way analogs (blue dashed line), the real dynamically cold disks, but the distribution of Milky Way analogs is slightly shifted to higher values. Analytical predictions for randomly oriented oblate (the gray line) and prolate (orange shaded area) ellipsoids, both assuming a Gaussian distribution $\mathcal{N}(\mu = 0.3, \sigma = 0.1)$ for the axial ratio $\xi \equiv c/a$, match the observations in remarkable detail. The transition of intrinsic shapes is associated with a change in the type of velocity anisotropy. While the local low-mass galaxies are suggested to possess tangentially biased stellar orbits, the stellar random motions of high-z low-mass galaxies are radially biased, probably along the predominant feeding filament of dark matter (D. Ceverino et al. 2015; V. Pandya et al. 2019, 2024a).

To conclude, the high-z populations recently observed by JWST are not dominated by dynamically cold disks supported by rotation, and their significant flattening is driven by anisotropy in stellar random motion. The ubiquitous florescence of rotation-supported disks may still remain a low-z phenomenon. JWST integral field spectroscopy for statistically significant samples of high-z galaxies will help to pin down their kinematic nature and intrinsic shapes in the future.

Acknowledgments

We appreciate the thoughtful and constructive comments by our reviewer. Y.P. and B.W. acknowledge the National Science Foundation of China (NSFC), grant Nos. 12125301, 12192220, and 12192222, and the science research grant from the China Manned Space Project, No. CMS-CSST-2021-A07.

Funding for the Sloan Digital Sky Survey IV has been provided by the Alfred P. Sloan Foundation, the U.S. Department of Energy Office of Science, and the participating Institutions. SDSS acknowledges support and resources from the Center for High Performance Computing at the University of Utah. The SDSS website is www.sdss.org.

SDSS-IV is managed by the Astrophysical Research Consortium for the Participating Institutions of the SDSS Collaboration, including the Brazilian Participation Group, Carnegie Institution for Science, Carnegie Mellon University, Chilean Participation Group, French Participation Group, Harvard–Smithsonian Center for Astrophysics, Instituto de Astrofísica de Canarias, Johns Hopkins University, Kavli Institute for the Physics and Mathematics of the Universe (IPMU)/University of Tokyo, Korean Participation Group, Lawrence Berkeley National Laboratory, Leibniz Institut für Astrophysik Potsdam (AIP), Max-Planck-Institut für Astronomie (MPIA Heidelberg), Max-Planck-Institut für Astrophysik (MPA Garching), Max-Planck-Institut für Extraterrestrische Physik (MPE), National Astronomical Observatories of China, New Mexico State University, New York University, University of Notre Dame, Observatário Nacional/MCTI, Ohio State University, Pennsylvania State University, Shanghai Astronomical Observatory, United Kingdom Participation Group, Universidad Nacional Autónoma de México, University of Arizona, University of Colorado Boulder, University of Oxford, University of Portsmouth, University of Utah, University of Virginia, University of Washington, University of Wisconsin, Vanderbilt University, and Yale University.

Data Availability

The measurements and quality assessments of stellar spin λ_{R_e} can be found in Table 1 of B. Wang & Y. Peng (2023). The measurements of ellipticity, photometric and kinematic position angles PA_{phot} and PA_{kine} are taken from the catalog of K. Zhu et al. (2023) available at https://manga-dynpop.github.io. The Sérsic indices are taken from the PyMorph photometric catalog (J.-L. Fischer et al. 2019; H. Domínguez Sánchez et al. 2022), published on https://www.sdss4.org/dr17/data_access/value-added-catalogs/?vac_id=manga-pymorph-dr17-photometric-catalog. Stellar mass and SFR of MaNGA galaxies are retrieved from GSWLC-X2 catalog (S. Salim et al. 2016, 2018) available on https://salims.pages.iu.edu/gswlc/.

ORCID iDs

Bitao Wang https://orcid.org/0000-0002-6137-6007
Yingjie Peng https://orcid.org/0000-0003-0939-9671
Michele Cappellari https://orcid.org/0000-0002-1283-8420
Hua Gao https://orcid.org/0000-0003-1015-5367

References

Abdurro'uf, Accetta, K., Aerts, C., et al. 2022, ApJS, 259, 35
Adamo, A., Atek, H., Bagley, M. B., et al. 2024, arXiv:2405.21054
Belokurov, V., Erkal, D., Evans, N. W., Koposov, S. E., & Deason, A. J. 2018, MNRAS, 478, 611
Bertola, F., & Capaccioli, M. 1975, ApJ, 200, 439
Bevacqua, D., Cappellari, M., & Pellegrini, S. 2022, MNRAS, 511, 139
Binney, J. 1976, MNRAS, 177, 19
Binney, J. 1978, MNRAS, 183, 501
Binney, J. 1985, MNRAS, 212, 767
Binney, J. 2005, MNRAS, 363, 937
Bundy, K., Bershady, M. A., Law, D. R., et al. 2015, ApJ, 798, 7
Cappellari, M. 2002, MNRAS, 333, 400
Cappellari, M. 2013, ApJL, 778, L2
Cappellari, M. 2016, ARA&A, 54, 597
Cappellari, M. 2017, MNRAS, 466, 798
Cappellari, M., Emsellem, E., Bacon, R., et al. 2007, MNRAS, 379, 418
Cappellari, M., McDermid, R. M., Alatalo, K., et al. 2013a, MNRAS, 432, 1862
Cappellari, M., Scott, N., Alatalo, K., et al. 2013b, MNRAS, 432, 1709
Ceverino, D., Primack, J., & Dekel, A. 2015, MNRAS, 453, 408
Cleveland, W. S., & Devlin, S. J. 1988, JASA, 83, 596
Dekel, A., Ginzburg, O., Jiang, F., et al. 2020, MNRAS, 493, 4126
Domínguez Sánchez, H., Margalef, B., Bernardi, M., & Huertas-Company, M. 2022, MNRAS, 509, 4024
Drory, N., MacDonald, N., Bershady, M. A., et al. 2015, AJ, 149, 77
Emsellem, E., Cappellari, M., Krajnović, D., et al. 2007, MNRAS, 379, 401
Emsellem, E., Cappellari, M., Krajnović, D., et al. 2011, MNRAS, 414, 888
Emsellem, E., Monnet, G., & Bacon, R. 1994, A&A, 285, 723
Faber, S. M., Tremaine, S., Ajhar, E. A., et al. 1997, AJ, 114, 1771
Ferreira, L., Conselice, C. J., Sazonova, E., et al. 2023, ApJ, 955, 94
Finkelstein, S. L., Bagley, M. B., Ferguson, H. C., et al. 2023, ApJL, 946, L13
Fischer, J.-L., Domínguez Sánchez, H., & Bernardi, M. 2019, MNRAS, 483, 2057
Fraser-McKelvie, A., Cortese, L., van de Sande, J., et al. 2021, MNRAS, 503, 4992
Fujimoto, S., Ouchi, M., Kohno, K., et al. 2024, arXiv:2402.18543
Gao, H., Ho, L. C., Barth, A. J., & Li, Z.-Y. 2020, ApJS, 247, 20
Graham, M. T., Cappellari, M., Li, H., et al. 2018, MNRAS, 477, 4711
Harborne, K. E., Power, C., Robotham, A. S. G., Cortese, L., & Taranu, D. S. 2019, MNRAS, 483, 249
Harikane, Y., Inoue, A. K., Ellis, R. S., et al. 2024, arXiv:2406.18352
Hubble, E. P. 1926, ApJ, 64, 321
Hubble, E. P. 1936, Realm of the Nebulae (New Haven, CT: Yale Univ. Press)
Illingworth, G. 1977, ApJL, 218, L43
Kartaltepe, J. S., Rose, C., Vanderhoof, B. N., et al. 2023, ApJL, 946, L15
Kormendy, J., & Bender, R. 1996, ApJL, 464, L119
Krajnović, D., Cappellari, M., De Zeeuw, P. T., & Copin, Y. 2006, MNRAS, 366, 787
Krajnović, D., Emsellem, E., Cappellari, M., et al. 2011, MNRAS, 414, 2923
Krajnović, D., Ural, U., Kuntschner, H., et al. 2020, A&A, 635, A129
Lagos, C. d. P., Emsellem, E., van de Sande, J., et al. 2022, MNRAS, 509, 4372
Law, D. R., Cherinka, B., Yan, R., et al. 2016, AJ, 152, 83
Li, H., Mao, S., Cappellari, M., et al. 2018, ApJL, 863, L19
Mo, H., Chen, Y., & Wang, H. 2024, MNRAS, 532, 3808
Padilla, N. D., & Strauss, M. A. 2008, MNRAS, 388, 1321
Pandya, V., Loeb, A., McGrath, E. J., et al. 2024a, arXiv:2407.17552
Pandya, V., Primack, J., Behroozi, P., et al. 2019, MNRAS, 488, 5580
Pandya, V., Zhang, H., Huertas-Company, M., et al. 2024b, ApJ, 963, 54
Pillepich, A., Nelson, D., Springel, V., et al. 2019, MNRAS, 490, 3196
Pillepich, A., Sotillo-Ramos, D., Ramesh, R., et al. 2023, arXiv:2303.16217
Rodríguez, S., & Padilla, N. D. 2013, MNRAS, 434, 2153
Rowland, L. E., Hodge, J., Bouwens, R., et al. 2024, arXiv:2405.06025
Salim, S., Boquien, M., & Lee, J. C. 2018, ApJ, 859, 11
Salim, S., Lee, J. C., Janowiecki, S., et al. 2016, ApJS, 227, 2
Sánchez-Janssen, R., Méndez-Abreu, J., & Aguerri, J. A. L. 2010, MNRAS, 406, L65
Sandage, A., Freeman, K. C., & Stokes, N. R. 1970, ApJ, 160, 831
Santucci, G., Brough, S., van de Sande, J., et al. 2022, ApJ, 930, 153
Santucci, G., Brough, S., van de Sande, J., et al. 2023, MNRAS, 521, 2671
Sun, W., Ho, L. C., Zhuang, M.-Y., et al. 2024, ApJ, 960, 104
Tacchella, S., Diemer, B., Hernquist, L., et al. 2019, MNRAS, 487, 5416
Thob, A. C. R., Crain, R. A., McCarthy, I. G., et al. 2019, MNRAS, 485, 972
Tomassetti, M., Dekel, A., Mandelker, N., et al. 2016, MNRAS, 458, 4477
Trayford, J. W., Frenk, C. S., Theuns, T., Schaye, J., & Correa, C. 2019, MNRAS, 483, 744
van de Sande, J., Croom, S. M., Bland-Hawthorn, J., et al. 2021a, MNRAS, 508, 2307
van de Sande, J., Scott, N., Bland-Hawthorn, J., et al. 2018, NatAs, 2, 483
van de Sande, J., Vaughan, S. P., Cortese, L., et al. 2021b, MNRAS, 505, 3078

van der Wel, A., Rix, H.-W., Holden, B. P., Bell, E. F., & Robaina, A. R. 2009, ApJL, 706, L120
Vega-Ferrero, J., Huertas-Company, M., Costantin, L., et al. 2024, ApJ, 961, 51
Wang, B., Cappellari, M., & Peng, Y. 2021, MNRAS, 500, L27
Wang, B., Cappellari, M., Peng, Y., & Graham, M. 2020, MNRAS, 495, 1958
Wang, B., & Peng, Y. 2023, ApJL, 950, L22
Wang, B., Peng, Y., & Cappellari, M. 2023, NatAs, submitted
Weijmans, A.-M., de Zeeuw, P. T., Emsellem, E., et al. 2014, MNRAS, 444, 3340
Wisnioski, E., Förster Schreiber, N. M., Wuyts, S., et al. 2015, ApJ, 799, 209
Xu, D., Gao, H., Bottrell, C., Yesuf, H. M., & Shi, J. 2024, arXiv:2407.19152
Zhang, H., Primack, J. R., Faber, S. M., et al. 2019, MNRAS, 484, 5170
Zhu, K., Lu, S., Cappellari, M., et al. 2023, MNRAS, 522, 6326